Modeling the early stages of reactive wetting

Daniel Wheeler,* James A. Warren, and William J. Boettinger
Metallurgy Division, Material Measurement Laboratory, National Institute of Standards and Technology, Gaithersburg, Maryland 20899, USA
(Received 28 June 2010; published 9 November 2010)

Recent experimental studies of molten metal droplets wetting high-temperature reactive substrates have established that the majority of triple-line motion occurs when inertial effects are dominant. In light of these studies, this paper investigates wetting and spreading on reactive substrates when inertial effects are dominant using a thermodynamically derived diffuse interface model of a binary three-phase material. The liquid-vapor transition is modeled using a van der Waals diffuse interface approach, while the solid-fluid transition is modeled using a phase field approach. The results from the simulations demonstrate an $O(t^{-1/2})$ spreading rate during the inertial regime and oscillations in the triple-line position when the metal droplet transitions from inertial to diffusive spreading. It is found that the spreading extent is reduced by enhancing dissolution by manipulating the initial liquid composition. The results from the model exhibit good qualitative and quantitative agreement with a number of recent experimental studies of high-temperature droplet spreading, particularly experiments of copper droplets spreading on silicon substrates. Analysis of the numerical data from the model suggests that the extent and rate of spreading are regulated by the spreading coefficient calculated from a force balance based on a plausible definition of the instantaneous interface energies. A number of contemporary publications have discussed the likely dissipation mechanism in spreading droplets. Thus, we examine the dissipation mechanism using the entropy-production field and determine that dissipation primarily occurs in the locality of the triple-line region during the inertial stage but extends along the solid-liquid interface region during the diffusive stage.

DOI: 10.1103/PhysRevE.82.051601 PACS number(s): 68.08.Bc, 68.08.De, 64.70.D−, 64.70.F−

I. INTRODUCTION

Characterizations of metal alloys wetting and spreading on dissolving substrates typically assume that inertial effects are not dominant or that the majority of dissipation is due to viscous forces [1–4]. In many respects this seems an entirely reasonable approach since the majority of experiments do not capture the early time behavior when inertial effects are dominant but focus on the late-stage spreading when chemical diffusion dominates and substrate dissolution occurs. Typically, experimental studies measure only slow spreading on the order of seconds or even minutes for millimeter-sized metal droplets consistent with diffusion-dominated spreading [1,5–7]. However, using improved techniques, a number of recent experiments [7–10] capture the rapid early-stage spreading and demonstrate that the spreading duration is consistent with the inertial time scale [11]. The variations in experimental findings can be attributed to differences in substrate temperature, composition of the vapor phase influencing substrate oxidation, contact mechanisms between the substrate and molten droplet, camera shutter speed, as well as other factors [7]. An often important aspect of managing these factors is arresting the formation of a substrate ridge on which the triple line becomes attached, which can retard spreading considerably [5].

The spreading droplet is often characterized in terms of a velocity versus contact angle relationship where the velocity is scaled using the instantaneous Capillary number, $\mathrm{Ca}^* = U^* \nu / \gamma$, where U^* is the instantaneous spreading speed, ν is the liquid viscosity, and γ is the liquid-vapor interface energy. Saiz *et al.* postulated that the dissipation mechanism may not be due to viscous forces as previously understood [7,12]. Clearly, in cases where the dissipation mechanism is not due to viscous effects, Ca is no longer a useful quantity for characterizing the spreading and an alternative parameter is required. An effective "triple-line friction" derived from molecular kinetics theory is suggested by Saiz *et al.* that is independent of viscosity but still dependent on interface energy and the contact angle. A number of recent experimental studies [11] clearly show that a large proportion of the spreading is characterized entirely by the inertial time scale $(t_i = \sqrt{\rho R_0^3 / \gamma}$, where ρ is the liquid density and R_0 is the drop radius) with $U \sim t^{-1/2}$, which is much faster than typical viscous spreading laws [13]. Furthermore, molecular-dynamics studies of Ag-Ni and Ag-Cu systems seem to confirm the $t^{-1/2}$ dependence of the spreading rate even for relatively small droplets [14,15].

This paper employs a diffuse interface method in order to analyze the issues surrounding the inertial spreading regime and dissipation mechanism discussed above. The diffuse interface approach implicitly includes a wide range of phenomena and as such does not require a posited relationship between spreading rate and contact angle [16]. Villanueva *et al.* [4] used a diffuse interface method to model reactive wetting and clearly identified two separate spreading regimes: an initial viscous regime and a subsequent diffusive regime [2]. The viscous regime demonstrated excellent agreement with standard viscous spreading laws. Further work by these authors [4] employed the same model to examine the effects of dissolution on spreading by first recovering the nondissolutive hydrodynamic limit as a base state.

*daniel.wheeler@nist.gov

In the viscous regime they found the spreading to be independent of the diffusion coefficient but accelerated in the diffusive regime as the diffusion coefficient is increased. This paper outlines a similar process using the initial liquid concentration to vary the driving force for dissolution while maintaining a constant diffusion coefficient. The general consensus of the literature is that inertial spreading occurs more slowly in systems that exhibit dissolution than in immiscible systems that do not exhibit dissolution [1,17]. However, this is contradicted by a number of experiments for saturated and pure liquids that show that the spreading can be on similar time scale under certain experimental conditions [7,9].

The work of Villanueva *et al.* [4] considers droplets that do not exhibit inertial effects due to the small drop size, which is limited by the requirement of having a narrow interface ($\approx$1 nm). In contrast to Ref. [4], this work sacrifices the realistic interface width in an attempt to model a system that exhibits inertial effects. Due to the drop size restrictions, the inertial time scale used by Villanueva *et al.* is $t_i \approx 6\times 10^{-11}$ s and the Capillary time scale $t_c = \nu R_0/\gamma \approx 2\times 10^{-10}$ s. At these values, the extent of spreading during the inertial stage is limited and the characteristic inertial effects are suppressed by viscous forces. The Ohnesorge number, given by $\mathrm{Oh} = t_c/t_i$, quantifies the relative importance of inertial and viscous effects. Typically, millimeter-sized metal droplets are highly inertial in nature with $\mathrm{Oh} \approx 1\times 10^{-3}$. Characteristic inertial effects, such as triple-line position oscillations and large droplet curvature variations, are reduced for $\mathrm{Oh} > 0.01$ and eliminated for $\mathrm{Oh} > 1$ [18]. From Villanueva *et al.*, $\mathrm{Oh} \approx 0.3$ and in this work $\mathrm{Oh} \approx 6\times 10^{-3}$.

In our work, the parameters are chosen so that the simulations are physically relevant and resemble experimental systems. For such systems, a substantial proportion of the spreading often occurs during the inertial stage (approximately 50% of the total spreading in [7,9]) and, thus, the reactive stages of spreading cannot be considered in isolation from the inertial stage without first determining the extent of spreading during the inertial stage. Other authors have studied parameter regimes where dissolution is initially dominant [2,4], but for these regimes ($\mathrm{Oh} \approx 0.3$ and the diffusion time scale is closer to the Capillary time scale) the inertial stage of spreading is effectively masked.

Jacqmin makes an extensive study of the role of the diffuse interface method, specifically for a Cahn-Hilliard–van der Waals (CHW) system, in relieving the stress singularity that occurs for classical sharp interface methods [16]. Since the interface is diffuse, the CHW does not require an explicit alteration to the no-slip boundary condition to allow for triple-line slip. Jacqmin demonstrates that the CHW has the same far field and macroscopic behavior as classical hydrodynamic models of slip. Thus, in diffuse interface models that include hydrodynamics there is no need to define a slip length. The interface width determines both an effective slip length and the concentration profiles within the diffuse interface associated with adjustments to adsorption and desorption; these factors affect the evolution of the system in subtle ways. There is no exact expression relating interface width and the effective slip length; however, $\lambda = \delta/2R_0$ is suggested as a good rule of thumb of Ding and Spelt [19], where λ is the dimensionless effective slip length for a diffuse interface model. It is claimed that the slip length can be as large as 50 nm [20], which is close to the chosen interface width in the present work, although the drop radius is only 1 μm. The slip length is found by Ding and Spelt to influence the onset of oscillations that occur when the droplet transitions from the inertial stage to the diffusive stage. The critical value of $\mathrm{Re}^* = U^*\rho R_0/\nu$, for which oscillations occur is reduced with decreasing λ. Hocking and Davis [21] have demonstrated that there is no simple relationship between contact angle and velocity when the approach to equilibrium becomes oscillatory, which seems to be the case in a number of experimental and numerical studies of millimeter-sized droplets [8,9,18,19].

The code used for the numerical analysis in this paper is developed using the FiPy partial differential equation (PDE) solver [22]. The numerical code used for the model in this paper will be made available shortly after publication and can be obtained by contacting the authors. The underlying linear solvers and parallel capabilities are provided by the TRILINOS tool suite [23].

In Sec. II the governing equations are presented followed by a discussion of the associated dimensionless parameters in Sec. III. Results from the numerical solution of the governing equations outlined are presented in Sec. IV. Section V analyzes the results in the context of previous work and ends with a discussion of the dissipation mechanism. Section VI presents the conclusions. Appendix A derives the governing equations presented in Sec. II, while Appendix B presents details of the numerical methods.

II. GOVERNING EQUATIONS

In this section, the final forms of the governing equations are presented along with the associated thermodynamic parameters and functions. The full derivation of the governing equations is described in Appendix A. The system consists of a three-phase (solid, liquid, and vapor) binary alloy. The liquid-vapor system is modeled as a two component van der Waals fluid, while the solid-fluid system is modeled with a phase field description. The density field acts as the order parameter for the liquid-vapor transition. Thus, the system is fully characterized by the spatiotemporal evolution of the mass density of component 1, ρ_1, the mass density of component 2, ρ_2, the phase field, ϕ, as well as the barycentric velocity field $\vec{u}$, as determined through the momentum equation. The three-dimensional equations are reduced to two dimensions by imposing cylindrical symmetry about $r=0$. The initial configuration consists of a spherical droplet with a radius of 1 μm tangent to a solid substrate surrounded by a vapor. The incompressible approximation is not made in this work for numerical reasons outlined in Appendix B; all the phases are compressible. The solid is modeled as a very viscous fluid as in previous phase field reactive wetting studies [2,4]. As the total mass density, $\rho = \rho_1 + \rho_2$, appears so frequently in the equations, it is more convenient to use ρ and ρ_2 as the independent density variables. For economy in notation, we write spatial derivatives $\partial_i \equiv \partial/\partial x_i$ and

$\partial_i^2 \equiv \partial^2/\partial x_i^2$ and require that repeated indices are summed unless otherwise indicated. Note that although the equations are solved with cylindrical symmetry, the equations are presented in the following Cartesian forms:

(1) Continuity:

$$\frac{\partial \rho}{\partial t} + \partial_j(\rho u_j) = 0. \tag{1}$$

(2) Diffusion:

$$\frac{\partial \rho_2}{\partial t} + \partial_j(\rho_2 u_j) = \partial_j\left(\frac{M}{T}\partial_j(\mu_2^{NC} - \mu_1^{NC})\right). \tag{2}$$

(3) Phase:

$$\frac{\partial \phi}{\partial t} + u_j\partial_j\phi = \epsilon_\phi M_\phi \partial_j^2\phi - \frac{M_\phi}{T}\frac{\partial f}{\partial \phi}. \tag{3}$$

(4) Momentum:

$$\frac{\partial(\rho u_i)}{\partial t} + \partial_j(\rho u_i u_j) = \partial_j(\nu[\partial_j u_i + \partial_i u_j]) - \rho_1\partial_i\mu_1^{NC} - \rho_2\partial_i\mu_2^{NC} - \left(\epsilon_\phi T\partial_j^2\phi - \frac{\partial f}{\partial \phi}\right)\partial_i\phi, \tag{4}$$

where u_i is a velocity component, T is the temperature, and $M = \bar{M}\rho_1\rho_2/\rho^2$ is the chemical mobility, which is proportional to the diffusivity, D, as outlined in Eq. (14). The values of $\bar{M}$ and ν vary from the solid to the fluid phases with the interpolation scheme chosen to be

$$\bar{M} = \bar{M}_s^{\psi}\bar{M}_f^{1-\psi} \tag{5}$$

and

$$\nu = \nu_s^{\psi}\nu_f^{1-\psi}, \tag{6}$$

where $\psi = \phi^a$ with $a = 4$. The values used in the simulations for $\bar{M}_s$, $\bar{M}_f$, ν_s, and ν_f are in Table I. The choice of a is discussed in Sec. V C. The free energy per unit volume is postulated to have the form [24]

$$f = p(\phi)f_s + [1 - p(\phi)]f_f + W\phi^2(1-\phi)^2,$$

where W is the phase field barrier height and $p(\phi) = \phi^3(10 - 15\phi + 6\phi^2)$ represents a smoothed step function common in-phase field models [25]. The free energies per unit volume in the separate fluid and solid phases are given by

$$f_f = \frac{e_1\rho_1^2}{m^2} + \frac{e_{12}\rho_1\rho_2}{m^2} + \frac{e_2\rho_2^2}{m^2} + \frac{RT}{m}[\rho_1 \ln \rho_1 + \rho_2 \ln \rho_2 - \rho \ln(m - \bar{v}\rho)] \tag{7}$$

and

TABLE I. Various parameter values.

Parameter	Value	Unit
ν_f	2.0×10^{-3}	kg/(s m)
ν_s	2.0×10^{4}	kg/(s m)
ϵ_1	2.0×10^{-16}	$m^7/(K\ kg\ s^2)$
ϵ_2	2.0×10^{-16}	$m^7/(K\ kg\ s^2)$
T	6.5×10^{2}	K
m	1.18×10^{-1}	kg/mol
R	8.31	J/(K mol)
v_a	1.0	
e_1	-4.56×10^{-1}	$J\ m^3/mol^2$
e_2	-4.56×10^{-1}	$J\ m^3/mol^2$
$\bar{v}$	1.3×10^{-5}	m^3/mol
A_1	2.83×10^{4}	J/mol
A_2	5.64×10^{4}	J/mol
ρ_s^{ref}	7.84×10^{-5}	kg/m^3
B	2.02×10^{5}	J/mol
W	1.27×10^{5}	N/m^2
ϵ_ϕ	1.0×10^{-9}	N/K
M_ϕ	1.0×10^{4}	$K\ m^2/(N\ s)$
$\bar{M}_f$	1.0×10^{-7}	$kg\ s\ K/m^3$
$\bar{M}_s$	1.0×10^{-11}	$kg\ s\ K/m^3$
R_0	1.0×10^{-6}	m
δ	1.0×10^{-7}	m
ρ_l^{equ}	7.35×10^{3}	kg/m^3

$$f_s = \frac{A_1\rho_1}{m} + \frac{A_2\rho_2}{m} + \frac{RT}{m}(\rho_1 \ln \rho_1 + \rho_2 \ln \rho_2 - \rho \ln \rho) + \frac{B}{\rho m}(\rho_s^{ref} - \rho)^2, \tag{8}$$

where m is the molecular weight (assumed to be equal for each component), R is the gas constant, $\bar{v}$ is the exclusion volume due to the finite size of the atoms, B is the solid compressibility, ρ_s^{ref} is a reference density for the solid, and the $e_i\rho_i/m$ are the free-energy contributions per unit mole due to intermolecular attraction in the van der Waals model. The A_1 and A_2 are temperature dependent parameters related to the heat of fusion between the solid and fluid phases. Along with the free energy, the specification of the pressure and the nonclassical chemical potentials are required to fully define the systems

$$P = \rho_1\frac{\partial f}{\partial \rho_1} + \rho_2\frac{\partial f}{\partial \rho_2} - f, \tag{9}$$

$$\mu_1^{NC} = \frac{\partial f}{\partial \rho_1} - \epsilon_1 T\partial_j^2\rho_1, \tag{10}$$

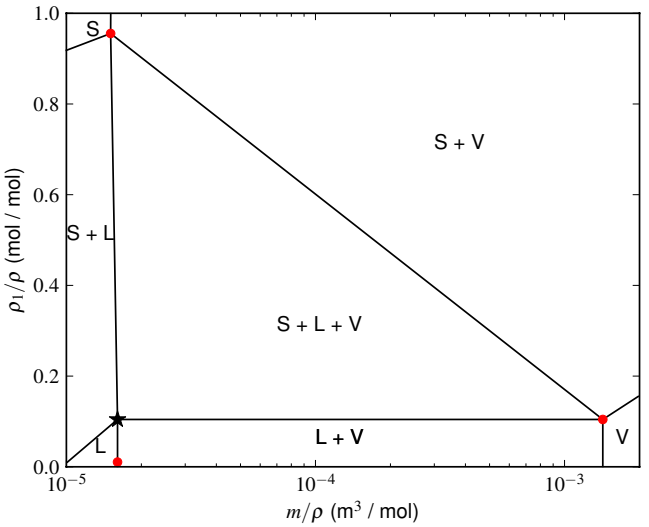

FIG. 1. (Color online) The phase diagram for the system of parameters presented in Table I. Each region represents a possible equilibrium state for a mixture of solid (s), liquid (l), and vapor (v) phases. The dots represent the initial conditions for the ξ=0.1 simulation discussed in Sec. IV. The star marks the liquid equilibrium condition. The liquid and vapor phases are rich in component 2, while the solid phase is rich in component 1.

$$\mu_2^{NC} = \frac{\partial f}{\partial \rho_2} - \epsilon_2 T \partial_j^2 \rho_2, \tag{11}$$

where ϵ_1 and ϵ_2 are free-energy gradient coefficients. The parameter values for Eqs. (1)–(11) are presented in Table I. The corresponding isothermal phase diagram for the molar fraction of component 1 versus the molar volume is displayed in Fig. 1.

Equations (1)–(4) are solved using a cell-centered collocated finite-volume scheme. The solution algorithm uses a fully coupled Krylov solver with Picard nonlinear updates using ρ_1, ρ_2, ϕ, and $\vec{u}$ as the independent variables. Further discussion of the numerical approach is given in Appendix B.

III. DIMENSIONLESS EQUATIONS AND TIME SCALES

It is useful for the purposes of analysis and completeness to clearly present the various dimensionless numbers and time scales that arise from solving Eqs. (1)–(4) in the context of spreading droplets. The dimensionless forms of Eqs. (2) and (4) are given by

$$\frac{\partial \rho_2}{\partial t} + \partial_j(u_j \rho_2) = \frac{1}{\mathrm{Pe}} \partial_j \left\{ \frac{\rho_1 \rho_2}{\rho^2} \partial_j [\mu_2 - \mu_1 - Q \partial_k^2 (\rho_2 - \rho_1)] \right\} \tag{12}$$

and

TABLE II. Complete list of time scales referred to in this paper.

Time scale	Symbol	Expression	Value (s)
Capillary	t_c	$\nu_f R_0 / \gamma_{lv}$	1.05×10^{-10}
Phase field	t_ϕ	$\delta^2 / \epsilon_\phi M_\phi$	1.0×10^{-9}
Inertial	t_i	$\sqrt{\rho_l^{\mathrm{equ}} R_0 / \gamma_{lv}}$	1.97×10^{-8}
Convection	t_a	R_0 / U	1.97×10^{-8}
Viscous	t_ν	$\rho_l^{\mathrm{equ}} R_0^2 / \nu_l$	3.68×10^{-6}
Interface diffusion	t_{diff}	$\delta^2 / 4K^2 D_f$	7.69×10^{-4}
Bulk diffusion	t_d	R_0^2 / D_f	1.04×10^{-3}
Solid deformation	t_s	$\delta \nu_s / \gamma_{lv}$	1.05×10^{-2}
Instantaneous convection	t_a^*	R_0 / U^*	

$$\frac{\partial(\rho u_i)}{\partial t} + \partial_j(\rho u_i u_j) = \frac{1}{\mathrm{Re}} \partial_j(\partial_j u_i + \partial_i u_j) - \frac{1}{\mathrm{Ma}^2} \partial_i P + \frac{1}{\mathrm{We}} (\rho_1 \partial_i \partial_j^2 \rho_1 + \rho_2 \partial_i \partial_j^2 \rho_2 - \tilde{\epsilon}_\phi \partial_i \phi \partial_j^2 \phi), \tag{13}$$

where the variables and operators are now dimensionless [the analysis of Eqs. (1) and (3) is not particularly revealing and is omitted]. For completeness, all the time scales referred to in this paper are displayed in Table II as a prerequisite for presenting the dimensionless numbers in Table III. It should be noted that in Table II, $U^* = U^*(t)$ is the instantaneous spreading speed and U is a fixed spreading speed posited *a priori*.

The time scale t_{diff} represents the time required for the solid-liquid interface to move a distance δ due to diffusion mediated melting or freezing. The expression for $t_{\mathrm{diff}} = \delta^2 / 4K^2 D_f$ is determined using an error function based similarity solution (see [26]) where $K(=-0.058)$ is the solution to

$$K + \left(\frac{X_1^l - X_1^{l,\mathrm{equ}}}{X_1^s - X_1^l} \right) \frac{\exp(-K^2)}{1 - \mathrm{erf}(K)} \frac{1}{\sqrt{\pi}} = 0$$

and the chemical-diffusion coefficient in the fluid, D_f, is defined by

$$D_f = \frac{\bar{M}_f R}{m \rho_l^{\mathrm{equ}}} = 9.58 \times 10^{-10} \ \mathrm{m^2/s}. \tag{14}$$

If we substitute R_0 for δ in the expression for t_{diff}, a rough estimate is obtained for complete equilibration of the system. The values of t_{diff} and t_i are derived using physically realistic values of $\bar{M}_f$, which constrain $t_{\mathrm{diff}} \gg t_i$. In this regime, the observable motion of the solid-liquid interface is negligible unless the simulations run for extremely long times or the simulations are equilibrated more rapidly by choosing an unphysical value for $\bar{M}_f$. During the development of the model, we simulated a number of parameter sets that exhibit dissolution, and we also verified that the simulations converge to accurate equilibrium configurations. The motion of the solid-

TABLE III. Relevant dimensionless numbers.

Parameter	Symbol	Expression	Value
Peclet number	Pe	$UR_0/D_f=t_d/t_a$	5.31×10^{4}
Reynolds number	Re	$UR_0\rho_l^{\mathrm{equ}}/\nu_f=t_\nu/t_a$	1.87×10^{2}
Weber number	We	$\mathrm{ReCa}=t_\nu t_c/t_a^2$	1.0
Mach number	Ma	U/c	5.72×10^{-2}
Unnamed	Q	$m\gamma_{lv}/RT\rho_l^{\mathrm{equ}}R_0$	5.64×10^{-2}
Effective dimensionless slip length	λ	δ/R_0	5.0×10^{-2}
Capillary number	Ca	$U\nu_f/\gamma_{lv}=t_c/t_a$	5.35×10^{-3}
Ohnesorge number	Oh	$\sqrt{\mathrm{Ca}/\mathrm{Re}}=t_c/t_i$	5.35×10^{-3}
Instantaneous Reynolds number	Re^*	$U^*R_0\rho_l^{\mathrm{equ}}/\nu_f=t_\nu/t_a^*$	
Instantaneous Capillary number	Ca^*	$U^*\nu_f/\gamma_{lv}=t_c/t_a^*$	

fluid interface due to dissolution is controlled by both diffusion (t_{diff}) and boundary kinetics (represented by t_ϕ). Here $t_\phi \ll t_i$, thus dissolution will be limited by diffusion rather than boundary kinetics. Additionally, solid-fluid interface motion due to hydrodynamic effects is negligible because the solid viscosity is chosen such that $t_s \gg t_i$, where t_s represents the time scale for discernible motion of the solid.

Table III presents the dimensionless numbers in terms of their constituent time scales where appropriate. Note that there are now two separate expressions for both the Reynolds number and the Capillary number based on U and U^*. By making an informed choice for the value of U, estimates are obtained for the likely values of the dimensionless numbers when using U^*. Here, $U=R_0/t_i=5.08\times10^{1}$ m/s is selected based on the spreading rate for a system that is dominated by inertial effects. The values of Oh, Re, and Pe in Table III all indicate that the interface energy and inertial forces dominate over viscous and diffusive forces. Since We=1, the interface energy and inertial forces are of approximately equivalent magnitude. Small values of Oh are representative of many experimental systems of technical interest: for example, Oh $\approx 2\times10^{-3}$ for a millimeter-sized droplet of copper and Oh $\approx 2\times10^{-2}$ for a micrometer-sized drop of lead.

Other dimensionless numbers (included for completeness) in Table III include the Mach number, Ma, which requires a definition for the speed of sound in the liquid, given by [27]

$$c = \sqrt{\left.\frac{\partial P}{\partial \rho}\right|_{\rho_l^{\mathrm{equ}}}} = 8.89\times10^{2}\ \mathrm{m/s}$$

and Q, which represents the ratio between interface and internal forces in the liquid droplet but has not been identified in the literature by the authors.

IV. RESULTS

In this section, we explore the rate and extent of droplet spreading based on variations in the initial liquid concentration and the Ohnesorge number. The initial liquid concentration determines the driving force for dissolution, while manipulating the Ohnesorge number influences the impact of inertial effects on spreading. The results presented here will provide the basis for comparison with other authors' work in Sec. V.

The extent of dissolution is established by decreasing the initial value of the liquid concentration, X_1^l, requiring the solid to dissolve in order to restore X_1^l to its equilibrium value, $X_1^{l,\mathrm{equ}}$. Explicitly, we set

$$X_1^l(t=0) = (1-\xi)X_1^{l,\mathrm{equ}},$$

$$\rho_l(t=0) = \rho_l^{\mathrm{equ}}, \tag{15}$$

where ξ defines a measure of the magnitude of the driving force for dissolution ($\xi<0$ induces freezing). When $\xi=0$, the system has no potential for dissolution, similar to pure hydrodynamic spreading where surface tension forcing dominates and interface motion is due only to convection as phase change is negligible. In this limit, comparisons can be made

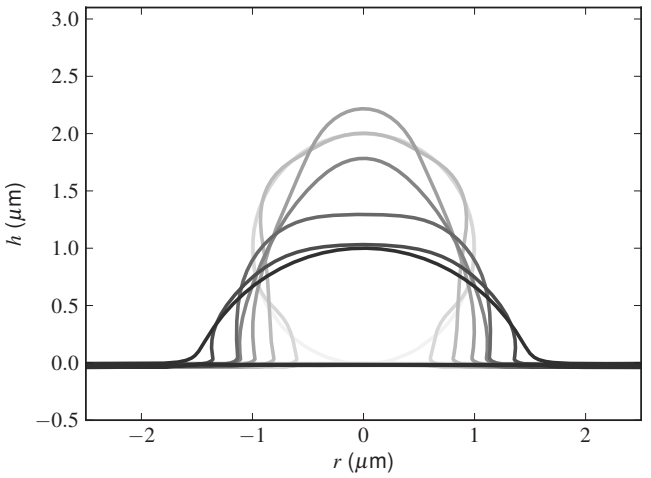

FIG. 2. Sequential configurations of the liquid-vapor and solid-fluid interfaces for $\xi=0$ and $\mathrm{Oh}=5.7\times10^{-3}$ with darker tones indicating later times. The curves demonstrate the extreme inertial effects on the droplet. The droplet starts as a sphere in tangent contact with the substrate. The drop height then rises considerably as the Capillary wave initiated from the triple line arrives at the top of the droplet. Although large amplitude ($\approx R_0/5$) oscillations occur in the triple-line position, the largest contact angle oscillation is only $\approx 0.03\pi$ rad.

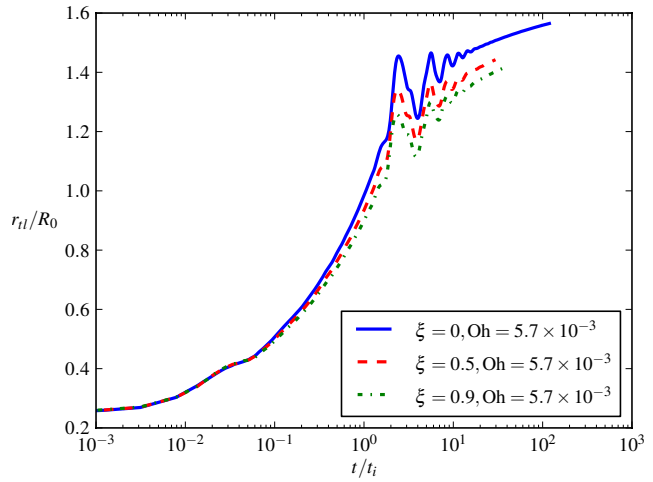

FIG. 3. (Color online) The spreading radius versus time for various values of ξ with $\mathrm{Oh}=5.7\times10^{-3}$. As ξ increases, the spreading rate and extent of spreading is slightly reduced.

with simpler spreading models and power laws. In addition to the hydrodynamic case (ξ=0), simulations were conducted with values of ξ=0.5 and ξ=0.9.

Figure 2 demonstrates the highly inertial nature of the spreading dynamics. Upon initiation of the simulation, pressure waves appear at the interface regions and travel through the interior of the droplet but then disperse quickly. Simultaneously, triple-line motion begins with a rapid change in the local contact angle but without any discernible motion elsewhere on the drop interface. This initiates the most noticeable feature of the spreading: a Capillary wave propagates from the triple line along the liquid-vapor interface, initiating the onset of the triple-line motion and progressing to the top of the droplet, causing a rapid rise in the drop height. The wave then travels back to the triple-line location while the droplet completes the majority of the spreading, with both events having a duration that corresponds to $\approx 2t_i$. During this interval, the triple-line motion is monotonic. On return to the triple-line location, the wave induces a reversal in the triple-line motion. Subsequent waves induce further reversals in the triple-line motion and the drop height with a period of $\approx 2t_i$. The amplitude of the oscillations diminishes in the manner of an underdamped oscillator, completing approximately five or six full cycles before ceasing entirely. Subsequently, very slow monotonic spreading occurs with the liquid-vapor interface appearing to have almost constant curvature.

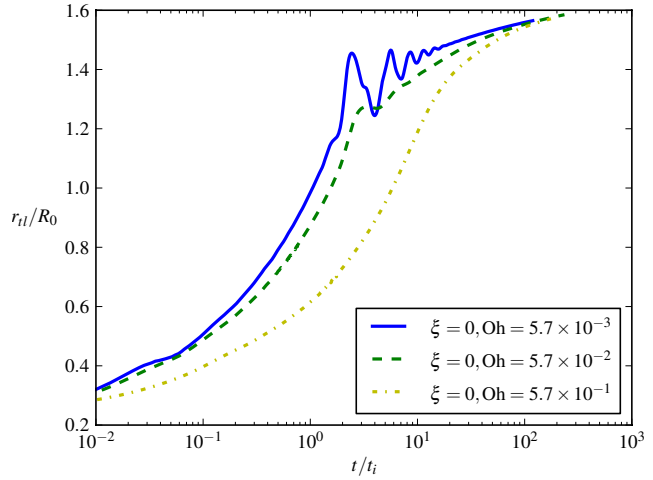

FIG. 4. (Color online) The spreading radius, r_{tl}, versus time for various values of Oh with ξ=0. The oscillations are eliminated for the largest value of Oh.

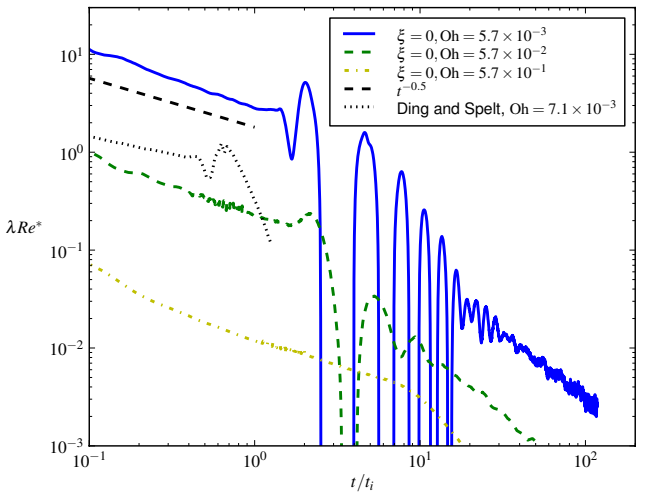

FIG. 5. (Color online) The dimensionless spreading rate against the dimensionless time with varying Oh and ξ=0. The spreading occurs in three distinct intervals. The sign changes in the solid curve correspond to the triple-line oscillations during the transition from the inertial to the diffusive regime.

Figures 3 and 4 display the scaled radial position of the triple line, r_{tl}/R_0, against the scaled time for varying values of ξ and Oh. The two intervals of fast and slow monotonic spreading can clearly be seen as well as the intervening period of oscillatory spreading as discussed in the previous paragraph. Increasing ξ reduces the extent of spreading, while increasing Oh eliminates the oscillations entirely and considerably reduces the spreading rate. In each of these cases, although the total amount of substrate dissolution is negligible (the solid-fluid interface moves less than $\delta/5$), there is a significant difference in the total spreading extent during the inertial and the subsequent reactive interface-equilibration stages. In Fig. 3, at early times ($t<0.1t_i$), the value of ξ has no impact on the spreading, but at later times ($t>0.1t_i$) the curves separate. When $t>10t_i$, the curves remain at a fixed distance apart. Increasing ξ not only results in a reduction in the extent of spreading but also results in a notable reduction in the amplitude of the oscillations. Figure 3 indicates that there is a 7% difference in the position of the triple line for the ξ=0 and the ξ=0.9 cases at $t=50t_i$. Equilibrium simulations (the results of which are not presented) demonstrate only 10% more spreading during the reactive stages. Thus, 7% is a significant difference in the initial starting condition for the dissolutive stage of spreading. In Fig. 4, the $\mathrm{Oh}=5.7\times10^{-1}$ curve separates from the other curves at very early times and has a greatly diminished spreading rate. Eventually, the curves become coincident at late times when the spreading is free of observable inertial manifestations for all values of Oh.

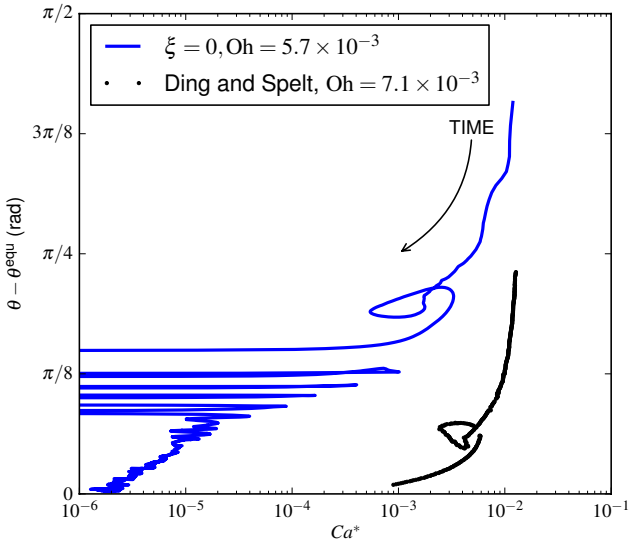

FIG. 6. (Color online) The observed contact angle against Ca^* for $\xi=0$ and $\mathrm{Oh}=5.7\times10^{-3}$.

In order to compare with other models, the radial position results presented in Fig. 4 are presented using a scaled spreading velocity in Fig. 5. The spreading velocity is scaled using a Reynolds number, $\lambda \mathrm{Re}^*$ ($\lambda=\delta/2R_0$), based on the interface width, δ, rather than using a standard Reynolds number based on the initial drop radius, R_0 [19]. The spreading velocity data used in Fig. 5 are smoothed to remove noise on the order of a grid spacing, the details of which are described in Appendix B. The sign changes in the blue curve, when $t_i<t<10t_i$, correspond to the triple-line oscillations seen in Fig. 4. The oscillations lie between intervals with monotonically decreasing spreading velocity. The $\mathrm{Oh}=5.7\times10^{-1}$ (yellow) curve exhibits a fairly steady decrease in velocity and then a much sharper reduction when $t\approx10t_i$, which corresponds to a slope change in Fig. 4. Note that the Oh values for simulations presented in Fig. 5 are manipulated by changing the value of ν_f only, and thus, a corresponding figure with no scaling for the spreading velocity would show only slight differences between the vertical positions of the curves.

Figure 6 displays the apparent contact angle, θ, against the Capillary number for $\mathrm{Oh}=5.7\times10^{-3}$ and $\xi=0$ demonstrating the convergence of θ to the nominal flat-interface equilibrium contact angle, θ^{equ}. The angle θ is calculated using techniques similar to those described by Villanueva *et al.* [4]. Although θ exhibits a hysteresis loop, it remains relatively steady during the period of oscillatory spreading and only varies by $\approx0.03\pi$ rad for the largest oscillation.

V. DISCUSSION

A. Comparison with other models

At early times, the flow is dominated by inertia and comparisons with theories of spreading on flat nonreactive substrates are fruitful. Indeed, an analytical spreading rate for the inertial regime can be derived (see [13]) and is given by $t^{-1/2}$. In Fig. 5, the slope of this power law (black dashed line) shows reasonable agreement with the $\mathrm{Oh}=5.7\times10^{-3}$ (blue curve) during the inertial regime. The vertical position of the black dashed line is selected to enable easy comparison with the blue curve.

In the work of Ding and Spelt [19], phase field and level set models of a spreading droplet are compared for a range of Ohnesorge numbers ($7.1\times10^{-3}\leq\mathrm{Oh}\leq2.8\times10^{-1}$) making it a useful study for comparing with our work. The black dotted curve in Fig. 5 is a digitized curve of the lowest value of Oh simulated by Ding and Spelt. This particular simulation is selected for display here as it manifests the most pronounced oscillations. They simulate droplets with an initial contact angle of $\pi/3$ rad and an equilibrium contact angle of $\pi/18$ rad using an effective dimensionless slip length of $\lambda=0.01$ ($\lambda=0.05$ in our work). Despite these differences, the overall motion of the droplets agrees well qualitatively for droplets with similar Ohnesorge numbers, although triple-line motion was not seen to reverse direction in their work. In Fig. 6, the contact angle experiences a hysteresis loop in a similar fashion to the work of Ding and Spelt, which is reproduced in the black dotted curve.

It has been conjectured [19,21] that the value of $\lambda \mathrm{Re}^*$ controls whether or not the spreading becomes oscillatory. In the simulations presented here, $\lambda \mathrm{Re}^*$ varies between 1 and 10 for the lowest value of Oh, but this is harder to determine for experimental systems. Hydrodynamic analysis of experimental data results in a slip length that can vary substantially for different materials (typically between 1 and 100 nm [7]). Using these bounds, a typical millimeter-sized metal drop results in $0.01<\lambda \mathrm{Re}^*<1$ assuming a spreading rate of 1 m/s (in this work the spreading rate is ≈50 m/s). It is interesting to note that for values of $\lambda \mathrm{Re}^*<0.1$, no oscillatory motion was seen in the work by Ding and Spelt [19]. From Schiaffino and Sonin [18] it is experimentally determined that the transition between underdamped oscillations to overdamped decay (no oscillations) occurs as Oh increases above 1×10^{-2}. This is seemingly confirmed in Fig. 4 where the curve that corresponds to $\mathrm{Oh}=5.7\times10^{-3}$ has multiple oscillations, while the curve for $\mathrm{Oh}=5.7\times10^{-1}$ has no oscillations.

B. Comparison with experiments

In Figs. 7 and 8 the triple-line radial position results from the present work for $\mathrm{Oh}=5.7\times10^{-3}$ are compared with experimental results from Saiz and Tomsia [7,11] and Protsenko *et al.* [9]. These experiments are conducted at a high temperature (1100 °C) and exhibit fast spreading, which is either absent or undocumented in many other reactive wetting experiments [28]. From Saiz and Tomsia, the experimental results are for Au and Cu droplets with an initial radius of 1 mm spreading on Ni and Mo substrates, respectively, while from Protsenko *et al.* the experiments are for Cu droplets of a similar size spreading on Si substrates. The reasonable quantitative agreement between the experimental and simulation results in Figs. 7 and 8 (within $\approx20\%$ for the Cu-Mo combination) suggests that the spreading in the experimental systems is predominantly inertial in nature [11].

The Cu on Mo spreading in Fig. 7 indicates oscillatory behavior at the end of the inertial regime, although there are

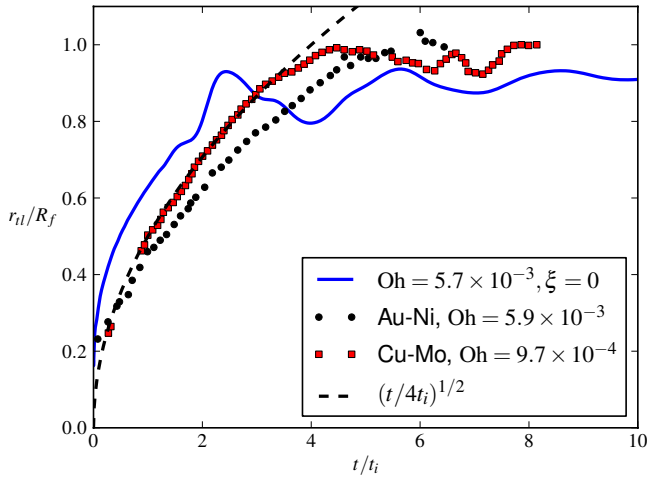

FIG. 7. (Color online) The radial position of the triple line scaled against the final radial position, R_f, against time (scaled with t_i) for ξ=0, Au-Ni experimental results, and Cu-Mo experimental results. The experimental results are digitized from Saiz *et al.* [7,11]. The inertial time scale, t_i, for the Au-Ni system is calculated using $\rho=1.1\times10^4$ kg/m^3, γ=1.0 J/m^2, and $R_0=1\times10^{-3}$ m. The inertial time scale for the Cu-Mo system is calculated using $\rho=8.9\times10^3$ kg/m^3, γ=1.3 J/m^2, and $R_0=1\times10^{-3}$ m. The values of t_i are 1.9×10^{-8} s for this work, 3.4×10^{-3} s for the Au-Ni system, and 2.6×10^{-3} s for the Cu-Mo system. This figure shows the reasonable agreement between the simulation and experimental data when scaled by the inertial time scale and the agreement with the $(t/4t_i)^{1/2}$ spreading rate.

only a handful of data points supporting this claim. Also, since the period of any oscillations is likely to be $\approx 2t_i$, a much greater duration of experimental data is required for confirmation. The dissolutive case (black solid curve) in Fig. 8 clearly demonstrates oscillations of a similar period, amplitude, and duration to the simulation results presented here

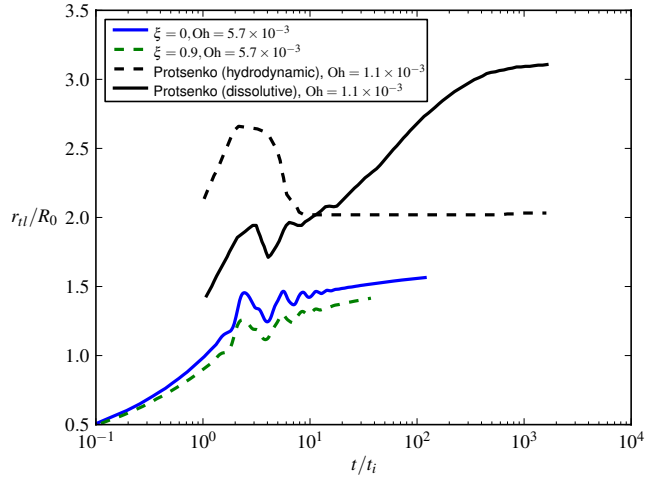

FIG. 8. (Color online) The spreading radius versus time for ξ=0 and ξ=0.9. The black curves are Cu-Si experiments digitized from Protosenko *et al.* The inertial time scale, t_i, for the Cu-Si system is calculated using $\rho=8.9\times10^3$ kg/m^3, γ=1.3 J/m^2, and $R_0=8.2\times10^{-4}$ m. The value of t_i is 1.9×10^{-8} s for this work and 2.0×10^{-3} s for the Cu-Si system.

as well as a contact angle hysteresis (not shown). It should be noted that oscillatory spreading also occurs in other systems such as water droplets on glass [18].

C. Nonequilibrium interface energy analysis

The driving force for spreading on a planar substrate is often characterized by the spreading coefficient given by

$$S^{\mathrm{equ}}(t) = \gamma_{sv}^{\mathrm{equ}} - [\gamma_{sl}^{\mathrm{equ}} + \gamma_{lv}^{\mathrm{equ}} \cos\ \theta(t)], \tag{16}$$

where the γ^{equ} are equilibrium values of the interface energies and θ is the observed contact angle. The utility of Eq. (16) is clearly limited to circumstances where the interface energies remain close to their equilibrium values during spreading. A number of authors [10,28–30] have suggested that this limitation may be overcome by replacing the equilibrium interface energies with their instantaneous values in Eq. (16). This yields a new spreading coefficient

$$\tilde{S}(t) = \tilde{\gamma}_{sv}(t) - [\tilde{\gamma}_{sl}(t) + \tilde{\gamma}_{lv}(t)\cos\ \theta(t)], \tag{17}$$

where the $\tilde{\gamma}$ are instantaneous interface energies. In principal, the use of $\tilde{\gamma}$ rather than γ^{equ} provides a more accurate description of the hydrodynamic driving force for spreading, particularly in the case where the time scale for spreading, t_i, is much faster than the interface equilibration time scale, t_{diff}. Since the solid-fluid interface remains planar over the time scales of interest in the simulations, using a horizontal force balance alone and ignoring the vertical imbalance when deriving Eq. (17) can be viewed as a reasonable assumption. An alternative expression to Eq. (17) can be derived if the solid-fluid interface is nonplanar using a more general Neumann's triangle horizontal and vertical force balance. In the following discussion, the expression used to calculate the $\tilde{\gamma}$ is described and then $\tilde{S}$ and S^{equ} are used to analyze the influence of ξ on the spreading dynamics.

It is a substantial advantage of our approach that we are able to develop an explicit expression for the instantaneous interface energies, allowing us to test the utility of $\tilde{S}$ as a metric for hydrodynamic spreading. In order to calculate $\tilde{S}$ using the results of the present calculations, we begin with two equivalent expressions for the equilibrium energy of a planar interface,

$$\gamma = \int_{-\infty}^{\infty} [\epsilon_1 T|\nabla\rho_1|^2 + \epsilon_2 T|\nabla\rho_2|^2 + \epsilon_\phi T|\nabla\phi|^2]dl$$

$$= 2\int_{-\infty}^{\infty} [f - f^\infty - \mu_1^\infty(\rho_1 - \rho_1^\infty) - \mu_2^\infty(\rho_2 - \rho_2^\infty)]dl, \tag{18}$$

where the ∞ superscript represents the value in the far field, and all the fields have equilibrium profiles. The equivalence of the expressions in Eq. (18) can be demonstrated by first writing down the Euler-Lagrange equation derived from the free-energy functional in Eq. (A3) with additional Lagrange multiplier terms for the conservation of both species and then integrating once. We now assert that a plausible measure of the instantaneous interface energy is

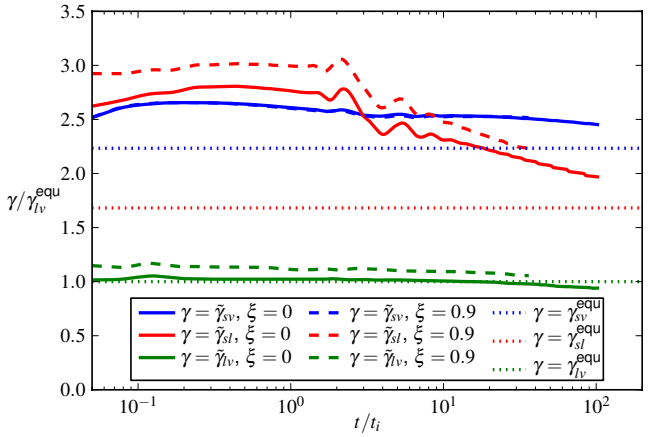

FIG. 9. (Color online) The instantaneous interface energies $\tilde{\gamma}$ plotted against time for ξ=0 and ξ=0.9. Both $\tilde{\gamma}_{lv}$ and $\tilde{\gamma}_{sl}$ are larger for the ξ=0.9 curve.

$$\tilde{\gamma}(t) = \int_l [\epsilon_1 T|\nabla\rho_1|^2 + \epsilon_2 T|\nabla\rho_2|^2 + \epsilon_\phi T|\nabla\phi|^2]dl, \quad (19)$$

where l is a line segment that both intersect and is normal to the interface being measured with $\int_l dl > \delta$. All fields in Eq. (19) are measured at time t. In general, the quantity $\tilde{\gamma}$ is a useful heuristic when the gradients are confined to the interface region. The numerical integration of Eq. (19) is conducted at a distance of 2δ from the triple-line location perpendicular to each local interface over a distance of 1.5δ. The integration points on the respective interfaces are chosen to be as near to the triple-line location as possible while avoiding the large variations in the value of $\tilde{\gamma}$ that occur close to the triple-line location [4]. Clearly, we could have defined another instantaneous interface energy as

$$\gamma^*(t) = 2\int_l [f - f^\infty - \mu_1^\infty(\rho_1 - \rho_1^\infty) - \mu_2^\infty(\rho_2 - \rho_2^\infty)]dl. \quad (20)$$

As one approaches equilibrium $\gamma^* \to \tilde{\gamma}$, but dynamically the quantities are different. It would appear that γ^* is less useful than $\tilde{\gamma}$, as γ^* requires the fields to be near the far field (equilibrium) values at the integration limit extremes for the value to "make sense" as an interface excess quantity. It is instructive to observe the $\tilde{\gamma}$ behavior over time (see Fig. 9). The values of $\tilde{\gamma}$ differ substantially from their equilibrium values for most of the simulation. The $\tilde{\gamma}_{sv}$ appears independent of ξ, which is a reasonable expectation, as ξ sets the liquid concentration. Increasing ξ results in an increase in both $\tilde{\gamma}_{lv}$ and $\tilde{\gamma}_{sl}$. In Fig. 9 large oscillations can be observed in the solid-liquid interface energy (red curve). These oscillations are due to the spatially varying values of $\tilde{\gamma}_{sl}$ along the solid-liquid interface in conjunction with the oscillations in the $\tilde{\gamma}_{sl}$ integration line location moving in unison with the triple-line location during the oscillatory phase of motion.

Using our definition of $\tilde{\gamma}$ and the apparent contact angle, θ, we can now calculate dynamic values of both $\tilde{S}$ and S^{equ}, which are presented in Fig. 10. The curves decrease rapidly from their maximum value, become negative at about $t=t_i$, and then oscillate in conjunction with the triple-line radial position oscillations.

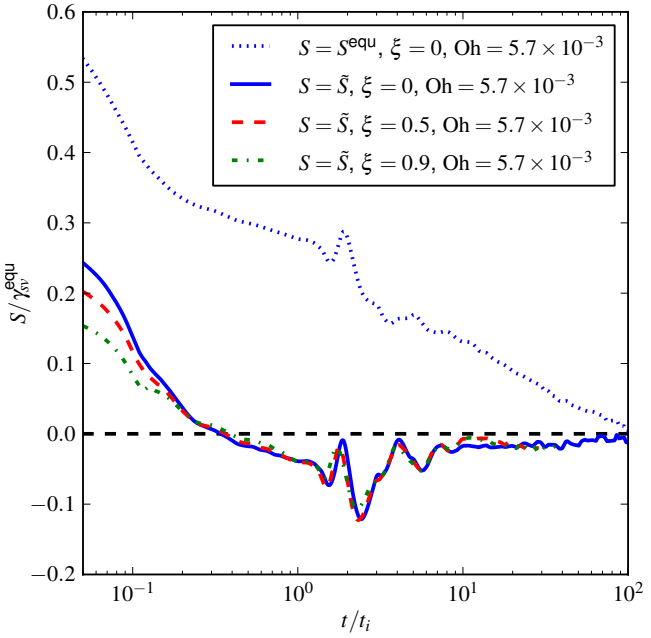

FIG. 10. (Color online) The scaled spreading coefficient versus scaled time for various values of ξ.

The quantity, $\tilde{S}$, is a measure of the hydrodynamic driving force for spreading and if the motion of the triple-line is reversed (as occurs in Fig. 3), this quantity is required to be negative. However, in Fig. 10 the values of $\tilde{S}$ tend to be overly negative. For example, $\tilde{S}$ switches relatively early to have negative values at $t=0.4t_i$ and has small negative values when $t>10t_i$. This is a systematic error caused by our arbitrary choice (2δ from the triple line) for the location of the integration points for the $\tilde{\gamma}$. Moving these locations closer to the triple line changes the $\tilde{S}$ to be more positive, while moving away from the triple line makes the values more negative. The quantity S has less intrinsic error as it only depends on the measured contact angle.

Eventually, the values of $\tilde{S}$ become quite small (<10% of its original value for ξ=0) although the drop is still spreading. Assuming $\tilde{S}$ quantifies the hydrodynamic driving force for spreading, then the differences in $\tilde{S}$ that occur for different values of ξ at early times may explain both the deviations observed in the spreading extent during the inertial regime ($t<t_i$) and the deviations in the oscillation amplitudes in Fig. 3. The small values of $\tilde{S}$ when compared with S^{equ} at late times suggest that the spreading has become quasistatic in nature and is bound to the evolving values of the $\tilde{\gamma}$. The evolution of the $\tilde{\gamma}_{sl}$ occurs on a time scale associated with t_{diff} while the hydrodynamic adjustment of the contact angle occurs on a time scale associated with t_i. Thus, the contact angle can adjust rapidly to balance the horizontal forces and suggests that the spreading is limited by interface equilibration at late times.

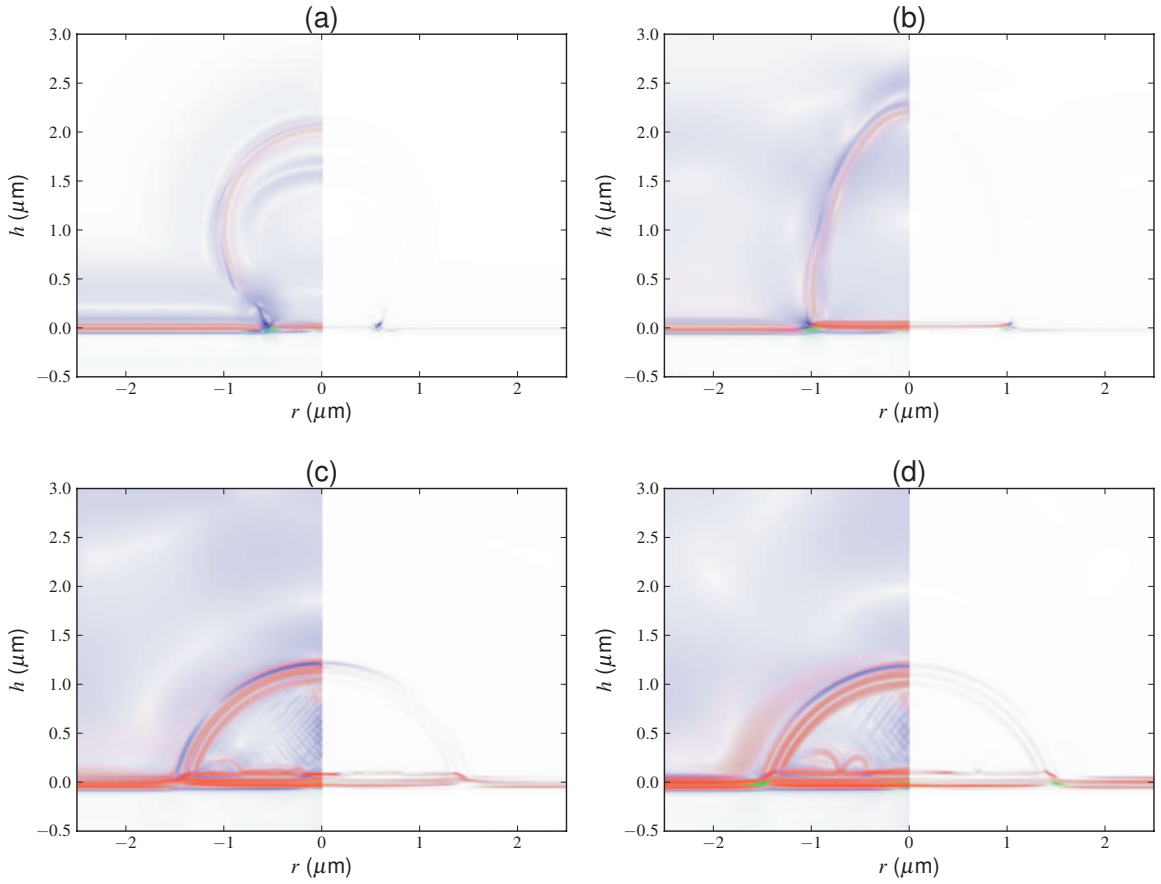

FIG. 11. (Color) Contour plots of the entropy production rate at (a) $t=0.1t_i$, (b) $t=t_i$, (c) $t=10t_i$, and (d) $t=20t_i$. The color intensity represents the magnitude of either $\sqrt[8]{\dot{S}_{\mathrm{PROD}}}$ on the left panel or $\sqrt{\dot{S}_{\mathrm{PROD}}}$ on the right panel. The colors represent the specific entropy production mechanism given by the terms in Eq. (21) (diffusive, phase field, and viscous), with red, green, and blue representing the first (diffusion), second (solid interface relaxation), and third (viscous flow) terms, respectively.

D. Dissipation analysis

Much of the literature surrounding droplet spreading is concerned with characterizing dissipation mechanisms from the point of view of an irreversible thermodynamic process [7,31,32]. In this spirit, this section provides an analysis of the entropy production, yielding the magnitudes of the various dissipation mechanisms in our model, which should, in turn, provide guidance on the formulation of simplified models. The expression used here for the total entropy production rate is given by [33]

$$\dot{S}_{\mathrm{PROD}} = \frac{M}{T^2}|\partial_j(\mu_1^{NC} - \mu_2^{NC})|^2 + \frac{M_\phi}{T^2}\left(\frac{\partial f}{\partial \phi} - \epsilon_\phi T \partial_j^2 \phi\right)^2 + \frac{\nu}{2T}(\partial_i u_j + \partial_j u_i)\partial_i u_j, \tag{21}$$

where each term in the sum is a distinct dissipation mechanism (diffusion, solid-fluid interface relaxation, and viscous flow).

The comprehensive overview of wetting by de Gennes [31] identified three main mechanisms for dissipation in spreading droplets: a viscous dissipation concerned with the "rolling motion" of the fluid within 100 μm of the triple line, a viscous dissipation in the precursor film, and a highly localized dissipation at the triple line associated with triple-line friction. In the present work, the precursor film is absent; however, both viscous dissipation in the bulk fluid and local triple-line dissipation are present but are conflated within the viscous dissipation term in Eq. (21). In most models of droplets spreading, the chosen model for slip relaxation at the triple line influences the underlying dissipation mechanism for the spreading droplet. For example, a molecular kinetics model of slip generally implies a local triple-line dissipation, while a hydrodynamic model of slip, such as Cox's model [34] or Tanner's law [35], both examples of de Gennes' rolling motion, implies nonlocalized dissipation [7,32]. We are reminded that this model employs diffuse interfaces, and thus no explicit slip condition is postulated, but such slip is a direct consequence of the model.

Figure 11 presents color contour plots of the entropy production rates at various times. The plots show the magnitude, location, and mechanism of entropy production for the nondissolutive case (the dissolutive cases are only slightly different). The color mapping is rescaled in Fig. 11 based on the $\max(\dot{S}_{\mathrm{PROD}})$ value for each image. For example, the total entropy production rate in Fig. 11(d) is only 0.4% of the value in Fig. 11(a). If we were considering a nonisothermal

system, there would be a further term in expression (21) containing temperature gradients, an effect not considered in this work.

At very early times (not shown), the entropy production is highly localized at the solid-fluid interface region as ϕ locally equilibrates. Subsequently (not shown), pressure waves are observed as the liquid-vapor interface equilibrates, and viscosity is the dominant mode of dissipation. By $t=0.1t_i$, the pressure waves have mostly subsided and the spreading is well under way. At this stage, the dominant dissipation mechanism remains viscous but is now highly localized at the triple line. As the inertial time scale is approached in Fig. 11(b), the dominant mechanism alternates between diffusive and viscous as the droplet oscillates during the $t_i<t<10t_i$ stage. The viscous dissipation remains highly localized at the triple line, while the diffusive dissipation mostly occurs in the solid-liquid interface with some occurring along the solid-vapor interface. This correlates with Fig. 9, which shows that the solid-liquid interface is far from local equilibrium until much later times. At later times [Fig. 11(c)], dissipation is mainly due to local interface equilibration along the solid-liquid and solid-vapor interface regions. The proportions of the numerically integrated value of $\int \dot{S}_{\mathrm{PROD}} dV$ for each term in Eq. (21) (diffusive, phase field, viscous) are (a) (0.51, 0.06, 0.43), (b) (0.73, 0.04, 0.23), (c) (0.84, 0.02, 0.14), and (d) (0.85, 0.07, 0.08) for each subplot in Fig. 11. These proportions demonstrate the growing influence of diffusive dissipation and the reduction in viscous dissipation as the system transitions from the inertial regime to the diffusive regime.

E. Remarks

The temporal adjustment to the equilibrium interface profiles is extremely complex and intimately related to the interface width and the interpolated values of the dynamic coefficients (ν and $\bar{M}$) [see Eqs. (5) and (6)]. The choice for the interpolation parameter a in Eqs. (5) and (6) biases the coefficients to have values close to the bulk fluid values in the interface region facilitating the fastest interface dynamics possible within the bounds set by the bulk values. The parameter a is tuned to a value of 4, as larger values do not increase the interface equilibration rate while smaller values considerably reduce the equilibration rate.

The equilibration of the density and phase field interface profiles is fast compared to that of the concentration field. The interface profile of the density field, ρ, is adjusted rapidly by hydrodynamics alone, while the interface profile of the concentration field, ρ_1/ρ, requires interdiffusion between the bulk phases and the interface regions. This compositional relaxation could, in principle, be as slow as the diffusion time scale, t_{diff} (see Table II), although the connection is imprecise, as this quantity is associated primarily with the motion of the interface due to dissolution (melting) rather than the relaxation of compositional profiles within the interface. The solid-fluid interfaces equilibrate slowly, compared to the liquid-vapor interface, as seen in Fig. 9. We expect that the observed interface relaxation time is unrealistic when compared with experimental studies of metallic systems, as our chosen interface width of $\delta=100$ nm is much larger than the $\delta\approx 1$ nm typical of metals. This is a shortcoming of this treatment and results in an unphysical time scale for local interface equilibration. Further analysis of the relationship between δ and the equilibration rate is required, though this analysis is beyond the scope of this work. The limitation of requiring $\delta/R\approx 0.1$ imposed by the available computation resources does not detract from the analysis presented in this section with respect to the reduced spreading when ξ is increased, the qualitative description of the spreading regimes and oscillations, or the quantitative comparisons with experiments.

VI. CONCLUSION

This paper presents results from a model of dissolutive spreading simulated in a parameter regime where inertial effects are initially dominant. The triple-line motion demonstrates good agreement with the $O(t^{-1/2})$ inertial spreading rate at early times. The model also generates oscillations that are characteristic of the transition from inertial to viscous or diffusive spreading. Subsequent analysis indicates that a force balance involving the instantaneous interface energies evaluated using the expression in Eq. (19) can explain the variation in spreading between the hydrodynamic and dissolutive cases. At late times, after inertial effects have ceased, the instantaneous spreading coefficient is close to zero suggesting that the local interface equilibration mechanism is controlling the spreading. Analysis of the dissipation mechanism via the entropy production expression demonstrates that dissipation occurs at the triple line during the inertial stage but transitions to the solid-fluid interfaces during the oscillatory stage consistent with the instantaneous interface energy analysis. Overall, the simulation results show good quantitative and qualitative agreement with a number of experimental results when time is scaled with the inertial time scale.

Modeling droplets that both have a realistic interface width and include inertial effects is impractical with current computational resources (at least for the model presented herein) and may require years of real time computation on large parallel clusters. In this work, to reduce the required computation time, the use of a realistic interface width has been sacrificed in order to preserve the inertial effects. This has the consequence of increasing the simulation time required for the local equilibration process across the solid-fluid interface as discussed in Sec. V C. Although this process has a longer duration than physically appropriate in the present work, a time regime over which the controlling mechanism for spreading is the local interface equilibration may be entirely physical. It is noted by Protsenko *et al.* [9] that the diffusive stage may occur in two separate parts. The first part is surmised to be the solid-liquid interface equilibration process and takes approximately one order of magnitude longer than the inertial time scale, which is faster than occurs here, but very similar in nature. The second part is the melting of the substrate, which is included in this model but only observed if the simulations are allowed to run for very long times or by choosing an unphysical value for the liquid diffusion coefficient.

Further work may involve both direct comparison with molecular kinetics theory and more detailed analysis of the impact of the interface width on the spreading dynamics.

ACKNOWLEDGMENTS

The authors would like to acknowledge the contributions of Dr. Jonathan E. Guyer and Dr. Walter Villanueva for their help and guidance in implementing the numerical model and analyzing the numerical data and Dr. Edmund B. Webb for insightful commentary and help in setting this work in the proper context.

APPENDIX A: DERIVATION OF THE GOVERNING EQUATIONS

In this section the underlying thermodynamic and constitutive relationships required for the derivation of Eqs. (2)–(4) are presented.

As previously outlined, the fluid phases are represented by a binary van der Waals equation of state and the solid phase is represented by a simple bulk modulus. The van der Waals equation of state is given by

$$\left(P - \frac{n^2}{V^2}(e_1 X_1 + e_2 X_2)\right)(V - \bar{v}n) = nRT, \tag{A1}$$

where X_1 and X_2 are the concentrations of each component, n is the number of moles, and $V/n = m/\rho$. All other parameters used in Eq. (A1) are defined in Sec. II. Equation (A1) can be related to the ideal-gas law but has modified pressure and volume terms to account for the long-range attraction of molecules and volume exclusion, respectively [24,36]. The solid equation of state is given by

$$PV_s = 2Bn\frac{V_s - V}{V_s}, \tag{A2}$$

where $V_s/n = m/\rho_s^{\mathrm{ref}}$. The Helmholtz free energies given in Eqs. (7) and (8) are derived from Eqs. (A1) and (A2), respectively, using the thermodynamic definitions given in Eqs. (9)–(11). In order to derive Eqs. (2)–(4), it is necessary to postulate a form for the free-energy functional.

As in Ref. [37], standard nonclassical diffuse interface expressions for ρ_1, ρ_2, and ϕ are used, which result in a functional of the form

$$F = \int \left[f + \frac{\epsilon_\phi T}{2}|\nabla\phi|^2 + \frac{\epsilon_1 T}{2}|\nabla\rho_1|^2 + \frac{\epsilon_2 T}{2}|\nabla\rho_2|^2 \right] dV. \tag{A3}$$

Using standard dissipation arguments [37], Eqs. (2) and (3) are derived using

$$\frac{\partial\phi}{\partial t} + u_j\partial_j\phi = -M_\phi\frac{\delta F}{\delta\phi}$$

and

$$\frac{\partial\rho_1}{\partial t} + \partial_j(u_j\rho_1) = -\partial_j J_{1,j}$$

and similarly for component (2). The fluxes are given by

$$J_{1,j} = -J_{2,j} = -M\partial_j\left(\frac{\mu_1^{NC} - \mu_2^{NC}}{T}\right),$$

where

$$\mu_1^{NC} = \frac{\delta F}{\delta\rho_1}$$

and

$$\mu_2^{NC} = \frac{\delta F}{\delta\rho_2}.$$

The form of the stress tensor required to derive the momentum equation is given by

$$\sigma_{ij} = \nu(\partial_j u_i + \partial_i u_j) + t_{ij}$$

using the standard assumption that the bulk viscosity, λ, is related to the shear viscosity via $\lambda = -\frac{2}{3}\nu$. The tensor, t_{ij}, is derived from a conservation law ($\partial_j t_{ij} = 0$) based on Noether's theorem [38]. The expression for t_{ij} is given by

$$t_{ij} = g^{NC}\delta_{ij} - \partial_j\rho\frac{\partial g^{NC}}{\partial(\partial_i\rho)}, \tag{A4}$$

where

$$g^{NC} = f^{NC} + \rho_1\lambda_1 + \rho_2\lambda_2. \tag{A5}$$

The quantity, g^{NC}, is the form of the free energy that includes Lagrange multipliers for conservation of species (1) and (2). The Lagrange multipliers for each species are equal to $\lambda_1 = -\mu_1^{NC}$ and $\lambda_2 = -\mu_2^{NC}$ in equilibrium using the variational derivative of $\int g^{NC}dV$ with respect to ρ_1 and ρ_2. Using Eqs. (A4) and (A5) the form for $\partial_i t_{ij}$ used in Eq. (4) can be derived,

$$\partial_j t_{ij} = -\rho_1\partial_i\mu_1^{NC} - \rho_2\partial_i\mu_2^{NC} + \partial_i\phi\frac{\delta F}{\delta\phi}. \tag{A6}$$

APPENDIX B: NUMERICAL APPROACH

In general, even for compressible systems, many conventional algorithms use the pressure field as the independent variable rather than the density field. This approach is thought to have more robust convergence properties [39] at low Mach numbers due to the weak dependence of pressure gradients on density, but the convergence properties deteriorate at higher Mach numbers. In this work, due to the nontrivial nature of the pressure-density relationship, an inversion of this relationship would be impractical, and it is more natural to solve for the density field rather than the pressure field. Due to the mesh collocation of the density and velocity fields, an interpolation scheme, known as the Rhie-Chow interpolation [40], is employed to ensure adequate velocity-pressure coupling.

The calculation of triple-line velocities is necessarily noisy, with fluctuations on a time scale of $\Delta x/U$, where Δx is the fixed grid spacing. In Fig. 5, the curves are constructed using a 20 point boxcar (equally weighted) averaging scheme collected at every ten time steps during the simula-

tion. We note that the sign changes in the blue curve ($t_i < t < 10t_i$) in Fig. 5 correspond to the triple-line oscillations and are *not* due to the averaging scheme. The velocity fluctuations will be small when U is large. Indeed, at early times, when $t/t_i < 1$, U is relatively large and the results are smooth. At later times, when $t/t_i > 10$, the averaging scheme does not smooth out the noise as the spreading rate is greatly reduced. This can be seen in the noisy behavior at long times for the $\mathrm{Oh} = 5.7 \times 10^{-3}$ curve (blue) in Fig. 5. The noise in the low velocity regime of Fig. 6 also reflects this behavior.

The measurements for θ are calculated using the tangent to the liquid-vapor interface at a distance of 1.3δ from the triple-line location. In general, this distance results in a reasonable approximation to the apparent contact angle.

1. Parasitic currents

Parasitic currents are a common source of numerical errors when computing flows with interface energy driving forces that have large Ca. Typically, for the systems of interest in this paper, $\mathrm{Ca} \approx 10^{-2}$, but parasitic velocities were still found to be a source of numerical error, particularly when trying to evaluate equilibrium solutions. Parasitic currents are characterized by quasisteady flow fields that do not dissipate over time despite the system reaching equilibrium in all other respects. This can result in equilibrium errors in both the density and concentration fields. Jamet *et al.* [41] as well as other researchers have demonstrated that parasitic currents can be eliminated by recasting the momentum equation in a form that only conserves momentum to the truncation error of the discretization rather than machine precision. The form of the momentum equation that eliminates parasitic currents is written in terms of the chemical potentials and is given by

$$\frac{\partial(\rho u_i)}{\partial t} + \partial_j(\rho u_i u_j) = \partial_j(\nu[\partial_j u_i + \partial_i u_j]) - \rho_1 \partial_i \mu_1^{NC} - \rho_2 \partial_i \mu_2^{NC} \tag{B1}$$

for binary liquid-vapor system. The discretized form of Eq. (B1) is known as an energy-conserving discretization in contrast to the momentum-conserving discretization, which results when the momentum equation is written in terms of the pressure [see Eq. (13)].

2. Convergence

Some simulations in this paper are tested for convergence with grid sizes of 180×125, 360×250, and 720×500 using the triple-line and drop height positions against time as the metrics for convergence. Production runs for the results presented use 360×250 grids. Details of these convergence tests can be obtained from the authors. Convergence at the nth time step is achieved when the kth iteration within the time step satisfies the residual condition $\beta_n^k / \beta_n^0 < 1 \times 10^{-1}$ for each of the equations where β_n^k is the L_2 norm of the residual at the kth iteration of the nth time step. Further decreases in the residual make little difference to the dynamic positions of the drop height and triple line. Numerical calculations indicate that, in the course of a simulation, Ma ranges from values that require compressible flow solvers (density based with $\mathrm{Ma} > 2 \times 10^{-1}$) to values for which compressible flow solvers have trouble with accuracy and convergence for traditional segregated solvers ($\mathrm{Ma} < 2 \times 10^{-1}$). The shift to low Ma generally occurs when the system is quite close to equilibrium and is not believed to affect the dynamic aspects of the simulation, which are of most interest in this paper. In general, for low Mach number flows, preconditioners are used to improve the convergence properties of segregated solvers. In this work, it was found that using a coupled solver along with a suitable preconditioner greatly improved the convergence properties. The preconditioners are available as part of the TRILINOS software suite [42]. The coupled convergence properties can be further improved by employing physics based preconditioners that change the nature of the equations based on the value of Ma [43] but are not used in this work.

[1] J. A. Warren, W. J. Boettinger, and A. R. Roosen, Acta Mater. **46**, 3247 (1998).

[2] W. Villanueva, K. Grönhagen, G. Amberg, and J. Ågren, Phys. Rev. E **77**, 056313 (2008).

[3] S. Su, L. Yin, Y. Sun, B. T. Murray, and T. J. Singler, Acta Mater. **57**, 3110 (2009).

[4] W. Villanueva, W. Boettinger, J. Warren, and G. Amberg, Acta Mater. **57**, 6022 (2009).

[5] E. Saiz, A. P. Tomsia, and R. M. Cannon, Acta Mater. **46**, 2349 (1998).

[6] R. Voitovitch, A. Mortensen, F. Hodaj, and N. Eustathopoulos, Acta Mater. **47**, 1117 (1999).

[7] E. Saiz and A. Tomsia, Nature Mater. **3**, 903 (2004).

[8] N. Grigorenko, V. Poluyanskaya, N. Eustathopoulos, and Y. Naidich, in *Interfacial Science in Ceramic Joining*, edited by A. Bellosi, T. Kosmac, and A. P. Tomsia (Springer, Dordrecht, 1998), Vol. 58 of NATO Advanced Science Institute Series, sub-series 3, High Technology, pp. 57–67.

[9] P. Protsenko, O. Kozova, R. Voytovych, and N. Eustathopoulos, J. Mater. Sci. **43**, 5669 (2008).

[10] L. Yin, B. T. Murray, S. Su, Y. Sun, Y. Efraim, H. Taitelbaum, and T. J. Singler, J. Phys.: Condens. Matter **21**, 464130 (2009).

[11] E. Saiz, A. P. Tomsia, N. Rauch, C. Scheu, M. Ruehle, M. Benhassine, D. Seveno, J. de Coninck, and S. Lopez-Esteban, Phys. Rev. E **76**, 041602 (2007).

[12] E. Saiz, R. M. Cannon, and A. P. Tomsia, Acta Mater. **48**, 4449 (2000).

[13] A.-L. Biance, C. Clanet, and D. Quéré, Phys. Rev. E **69**, 016301 (2004).

[14] E. B. Webb III, G. S. Grest, D. R. Heine, and J. Hoyt, Acta Mater. **53**, 3163 (2005).
[15] Y. Sun and E. B. Webb III, J. Phys.: Condens. Matter **21**, 464135 (2009).
[16] D. Jacqmin, J. Fluid Mech. **402**, 57 (2000).
[17] L. Yin, B. T. Murray, and T. J. Singler, Acta Mater. **54**, 3561 (2006).
[18] S. Schiaffino and A. A. Sonin, Phys. Fluids **9**, 3172 (1997).
[19] H. Ding and P. D. M. Spelt, J. Fluid Mech. **576**, 287 (2007).
[20] M. Schneemilch, R. A. Hayes, J. G. Petrov, and J. Ralston, Langmuir **14**, 7047 (1998).
[21] L. M. Hocking and S. H. Davis, J. Fluid Mech. **467**, 1 (2002).
[22] J. E. Guyer, D. Wheeler, and J. A. Warren, Comput. Sci. Eng. **11**, 6 (2009).
[23] M. A. Heroux *et al.*, ACM Trans. Math. Softw. **31**, 397 (2005).
[24] M. Plischke and B. Bergersen, *Equilibrium Statistical Physics* (World Scientific, Singapore, 1994).
[25] W. J. Boettinger, J. A. Warren, C. Beckermann, and A. Karma, Annu. Rev. Mater. Res. **32**, 163 (2002).
[26] W. J. Boettinger and G. B. McFadden, J. Phase Equilibria and Diffusion **31**, 6 (2010).
[27] L. D. Landau and E. M. Lifshitz, *Fluid Mechanics: Course in Theoretical Physics*, 2nd ed. (Pergamon Press, New York, 1987), Vol. 6.
[28] N. Eustathopoulos, Acta Mater. **46**, 2319 (1998).
[29] I. A. Aksay, C. E. Hoge, and J. A. Pask, J. Phys. Chem. **78**, 1178 (1974).
[30] S. Frenznick, M. Stratmann, and M. Rohwerder, Rev. Sci. Instrum. **79**, 043901 (2008).
[31] P. G. de Gennes, Rev. Mod. Phys. **57**, 827 (1985).
[32] F. Brochard-Wyart and P. de Gennes, Adv. Colloid Interface Sci. **39**, 1 (1992).
[33] R. Sekerka and Z. Bi, in *Interfaces for the 21st Century*, edited by M. K. Smith, M. J. Miksis, G. B. McFadden, G. P. Neitzel, and D. R. Canright (Imperial College Press, London, 2002), pp. 147–166.
[34] R. G. Cox, J. Fluid Mech. **168**, 169 (1986).
[35] L. H. Tanner, J. Phys. D **12**, 1473 (1979).
[36] C. Kittel and H. Kroemer, *Thermal Physics* (WH Freeman & Co, San Francisco, 1980).
[37] Z. Bi, and R. F. Sekerka, Physica A **261**, 95 (1998).
[38] D. M. Anderson, G. B. McFadden, and A. A. Wheeler, Annu. Rev. Fluid Mech. **30**, 139 (1998).
[39] J. H. Ferziger and M. Perić, *Computational Methods for Fluid Dynamics* (Springer, New York, 1996).
[40] C. M. Rhie and W. L. Chow, AIAA J. **21**, 1525 (1983).
[41] D. Jamet, D. Torres, and J. U. Brackbrill, J. Comput. Phys. **182**, 262 (2002).
[42] M. Heroux *et al.*, Sandia National Laboratories Technical Report No. SAND2003-2927, 2003 (unpublished).
[43] I. J. Keshtiban, F. Belblidia, and M. F. Webster, Department of Computer Science, Institute of Non-Newtonian Fluid Mechanics, University of Wales Technical Report, 2004 (unpublished).